Proceedings of the
Annual Stability Conference
Structural Stability Research Council
Atlanta, Georgia, April 21-24, 2020

A nondestructive method to find the buckling capacity for thin shells

Kshitij Kumar Yadav[1], Simos Gerasimidis[2]

Abstract
The presence of imperfections reduces the load carrying capacities of thin cylindrical shells significantly. This reduction depends on the size and the shape of imperfections—the vital information which is difficult and expensive to obtain. All cylinders contain imperfections in one form or another. And thus, the prediction of their buckling capacities is a daunting task that requires the accurate measurement of the imperfections—a difficult and expensive adventure. Due to the lack of inexpensive high-fidelity prediction method, thin cylindrical shells are designed by the highly conservative knockdown factor approach. Consequently, the full potential of the thin cylindrical shells is not being exploited. Recently, a nondestructive experimental method has been proposed to obtain the buckling capacity of thin cylindrical shells. In this method, lateral probing is utilized to find the post-buckling equilibrium configuration. The load-displacement profile of the probing carries substantial information, which characterizes the response of the imperfect thin cylindrical shells. This information can be used to obtain the buckling capacities of thin cylinders. In this study, we computationally testify this method and assess its practical feasibility. Local dimple-like imperfect thin cylinders are created, and their buckling capacities are found using two methods: the finite element method, and the newly proposed method using lateral probing. By comparing these two results, the accuracy of the proposed method is evaluated. Moreover, the effect of the location, with respect to the dimple, of probing is also investigated. Concomitantly, the interaction of more than one dimple and the lateral probing is explored to understand the fragility of the proposed method.

1. Introduction

Thin cylindrical shells are widely used structural elements due to their efficiency, ease of construction, and appeal to aesthetic. However, thin cylindrical shells are highly sensitive to imperfections, and their load carrying capacity is reduced significantly by the presence of even small imperfections (Koiter 1945). As a result, the inherent benefits associated with thin shells are shadowed, and this has long been an obstacle for the effective use of thin shells. The issue here is not only that imperfections reduce the capacity, but also that the imperfections induce the uncertainty. This means that it is difficult to predict the capacity of practical thin cylinders because the reduction in the load carrying capacity depends on the prior unknown parameters: the shape and the size of the imperfections-. To counter this uncertainty, design codes for thin cylinders are

[1] Graduate Research Assistant, University of Massachusetts Amherst, <kkyadav@umass.edu>
[2] Assistant Professor, University of Massachusetts Amherst, <sgerasimidis@umass.edu>

highly conservative, e.g., the Eurocode Part 1-6-2007. Theoretically, it is possible to measure the shape and the size of imperfections, but it is a time consuming and expensive enterprise, and thus not a viable alternative.

Recently, the evaluation of thin shells' exact capacity, without measuring the shape and the size of the imperfections present, received considerable attention (Thompson 2015, Thompson et al. 2016, Thompson et al. 2017, Hutchinson et al. 2017, Kreilos et al. 2017, Marthelot et al. 2017, Hutchinson et al. 2018, Fan 2019). This increased interest is attributed to the potential applications of thin shells in many emerging fields, e.g., flexible electronics, energy harvesting, etc. In these studies, a non-destructive method based on the energy barrier was proposed. The method exploits the energy landscape of thin cylindrical shells by probing the shells under different axial compression (Thompson 2015, Virot et al. 2017, Thompson et al. 2017). The load-displacement plots of the probe contain signatures of the energy-landscape (Virot et al. 2017), and this information can be utilized to estimates the capacity of cylinders. Thompson et al. (2015) have proposed this method, and Virot et al. (2017) have done experiments and demonstrated that there, indeed, is a relationship between the peak probing forces and corresponding axial compression.

In all the studies mentioned in the previous paragraph, the method was proposed but was not implemented or validated on imperfect thin cylinders. Fan (2019) has implemented the aforementioned method to find the buckling capacity of imperfect thin cylinders and has reported promising results. However, there are some uncertainties regarding the initial axial compression, he called it the prescribe axial load P_0, which is applied on the cylindrical shells before the probing. Fan (2019) has not given any clear recommendation on how to find the prescribe initial axial load P_0—very crucial information. The capacity of imperfect cylinders is unknown, and the prescribe axial load P_0 must be less than their capacity. And thus, we cannot rely on the uncertain definition of the initial prescribe axial load P_0.

In this study, we clearly define the initial prescribe axial load P_0, and propose an algorithm to find it. Once this crucial information is known, we use other steps of the proposed algorithm to find the axial capacity of imperfect thin cylindrical shells. The proposed algorithm is computationally validated on a perfect and two imperfect cylinders. For imperfect cylinders, we utilize the single and double dimples. Furthermore, the effect of the location of probing with respect to the imperfection is explored, and in the case of double dimples imperfect cylinder, the influence of locations of dimples is studied and enumerated.

2. Description of the Proposed Algorithm

In past studies, it was hypothesized that by probing thin cylinders under different axial compression (that is less than the critical axial compression) the capacity of thin shells can be predicted. The key element of the hypothesis is the energy barrier—the required energy for shifting the axially compressed thin cylinders to the post-buckling configuration from the pre-buckling configuration. A probe is used to shift the pre-buckling configuration to the post-buckling configuration, and the probing force-displacement can be exploited for the prediction of thin cylinders' capacity. Based on these studies, we propose an algorithm to predict the thin cylinders' capacity. The proposed algorithm has three steps: 1) finding the initial prescribe axial load P_0, 2) probing the axially compressed cylinder for different values of axial compression, and 3) collecting

the maximum probing loads and predicting the buckling capacity. Fig. 1 shows the flowchart of the algorithm.

In Step I, first the capacity of the perfect cylinder P_{cr} is found, then the knockdown factor k is evaluated. Next, the cylinder is put under the axial compression $P = 0.5kP_{cr}$, and the probing force F is applied. If the probing force F reaches a maximum and starts reducing, the P will be the initial prescribe axial load P_0 and Step I is completed; otherwise, the axial compression P is increased by 5 %, and again the probing force F is applied and traced. This loop is continued until we find the axial compressive force under which the probing force F reaches a maximum and starts reducing. The output of Step I is the initial prescribe axial load P_0—the minimum axial compression for which the probing force F reaches a maximum and starts reducing. The initial prescribe axial load P_0 is the input for step II. In step II, we put the cylinder under 11 axial compressions, i.e., $(1 + .025)^0 \times P_0$, $(1 + .025)^1 \times P_0$, $(1 + .025)^2 \times P_0$, …. $(1 + .025)^{10} \times P_0$. In all 11 cases, the cylinder is probed, and probing forces-displacement data is collected. Next, the maximum probing force F_{max} is extracted for all the 11 cases. In step III, the plot is drawn between the F_{max} (x axis) and corresponding axial compressions P (y axis). After that, using linear interpolation, the best fit line's equation is determined. The value of the y axis corresponds to the intersection of the line with the y axis is the predicted capacity of the cylinder.

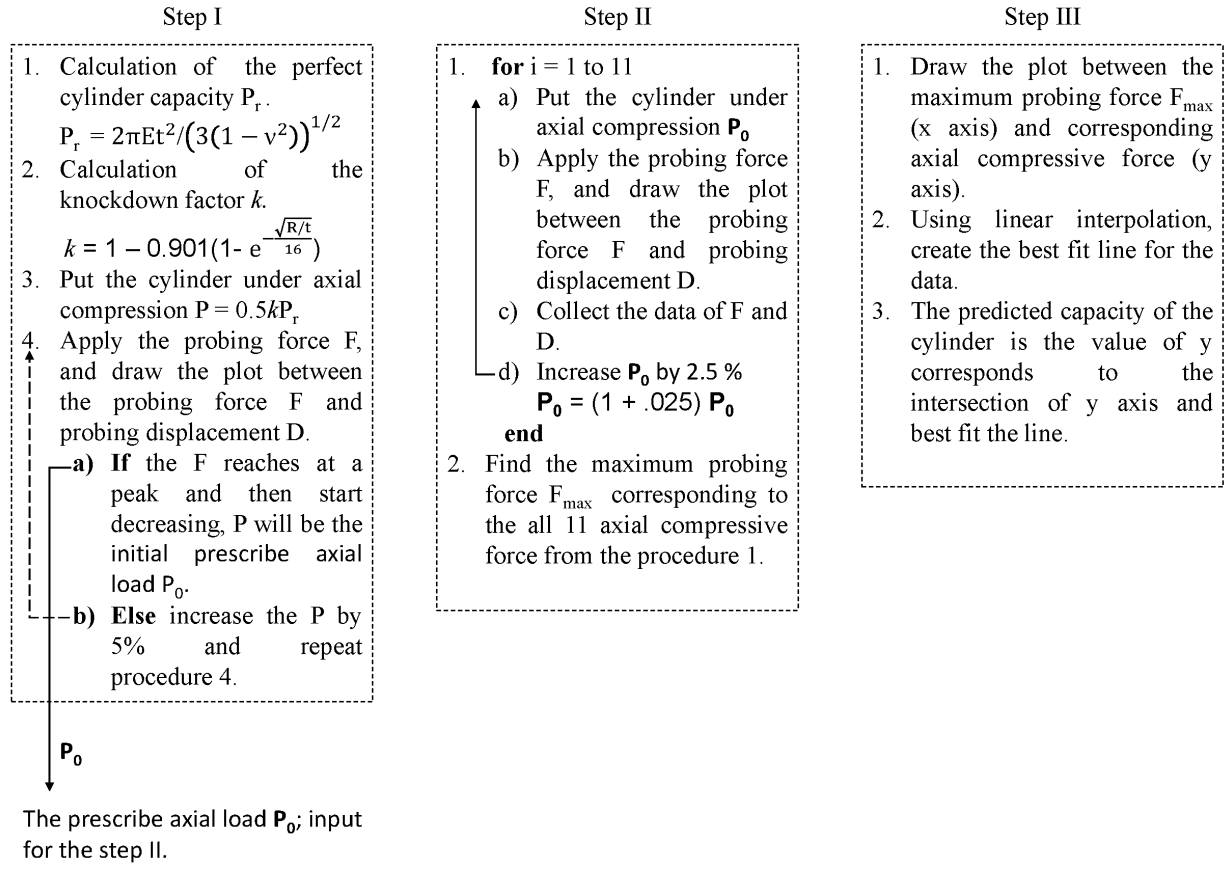

Figure 1: Flowchart of the proposed algorithm; there are three steps in this algorithm. In Step I, the initial prescribed axial load P_o is found; in Step II, 11 data of maximum probing force F_{max} is collected corresponds to axial compressions $(1 + .025)^0 \times P_0$, $(1 + .025)^1 \times P_0$, $(1 + .025)^2 \times P_0$, …. $(1 + .025)^{10} \times P_0$; in Step III, linear interpolation of F_{max} and axial compression is used to predict the capacity of the cylinder.

3. Application of the Algorithm on a Perfect Cylinder

In this study, we are limited to the computational implementation of the proposed algorithm, and the experimental implementation is not reported. First, we apply the algorithm on a perfect cylinder to assess the accuracy of the predicted capacity by comparing it with the actual capacity that is known. For this purpose, we chose the cylinder used by Gerasimidis et al. (2018) assuming linearly elastic material behavior. The dimensions and the material properties of the cylinder are given in Table 1.

Table 1: Dimensions and the material properties of the cylinder

Radius R (in)	Length L (in)	R/t	E (Psi)	N
9	31	225	10.6	0.3

3.1 Finite Element Modeling

All the analyses are performed in ABAQUS using the arch-length based Riks method (Riks 1979). For meshing, around 20000 four node reduced integration shell (S4R) elements are created, utilizing four integration points along the thickness of each element. The proposed algorithm has two parts: first, the cylinder is put under the prescribed axial compression, and second, the application of the probing force on the compressed cylinder. Fig. 2 demonstrates the Finite Element Modeling. For compressing the cylinder to a prescribed axial compression, two nodes are defined at the center of the top and bottom cross-sections of the cylinder; we call them center nodes. Rigid links are created to connect the nodes at the end of the cylinder to the respective center nodes to constrain the displacements U_1, U_2, and U_3, and rotations UR_1, UR_2, and UR_3 of the nodes at the end from moving and rotating with respect to the center nodes. Using these constraints one end of the cylinder is clamped by fixing the central node at z = 0. At the other end (z = L) a clamped boundary condition is enforced, but the end of the cylinder is loaded by applying an axial displacement $U_3 = -\Delta$ till the axial compression reached the prescribed value as shown in Fig. 2a. Once the cylinder is loaded under the prescribe axial compression, the probing force, directed toward the center of the cross-section, is applied in the middle of the cylinder as shown in Fig. 2b. With this description of finite element modeling, we will discuss the results in the next subsection.

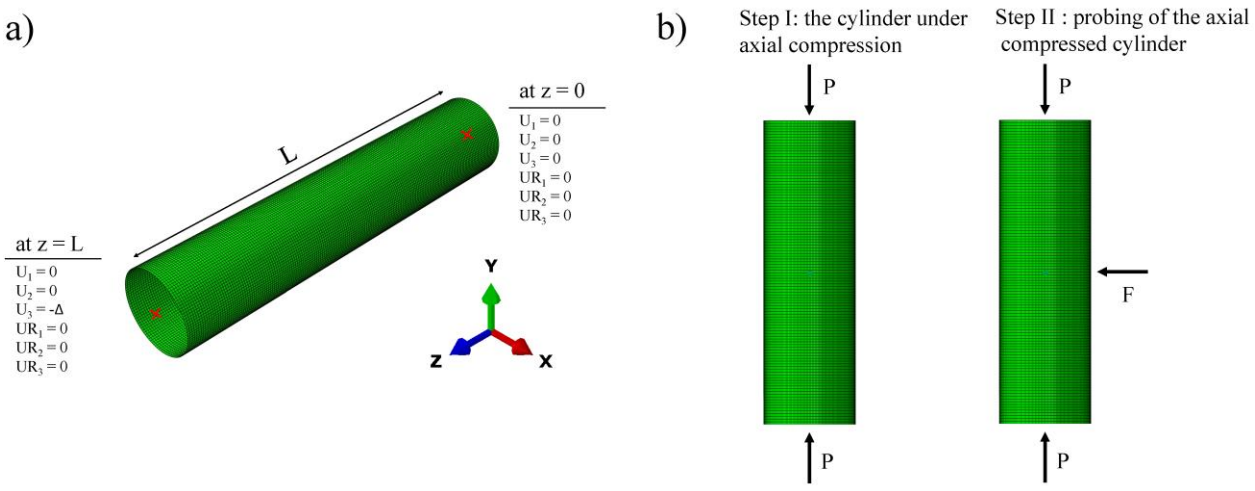

Figure 2: a) Finite element modeling and boundary conditions. b) Application the axial compression P and probing force F.

3.2 Prediction of the perfect cylinder's capacity

The application of Step I of the algorithm on the perfect cylinder results in the initial prescribed axial load P_0 = 1.4571e+04 lbf. This initial prescribed axial load P_0 is the input for Step II. In Step II, we put the cylinder under 11 different prescribed axial compression $P = (1 + .025)^0 \times P_0$, $(1 + .025)^1 \times P_0$, $(1 + .025)^2 \times P_0$, …. $(1 + .025)^{10} \times P_0$; thereafter, the probing force is applied at the middle of all the 11 axially compressed cylinders. In Fig. 3a, the plots between probing forces F and the probing displacements D are drawn for the 11 axially compressed cylinders. The maximum probing force F_{max} is reducing with the increase of the axial compression; it is expected as the energy barrier is reduced with the increase of axial compress (Virot et al. 2017)—less and less energy is required to shift the pre-buckling configuration to the post-buckling configuration as axial compression increases. In Fig. 3b, scatter plot is drawn between maximum probing force F_{max} and corresponding prescribed axial compression. These data are fitted by the line and the equation of the line is:

$$P = -1184F_{max} + 5.559\, e^{04} \quad (1)$$

The predicted capacity of the cylinder is the value of the P (y axis) corresponds to the value of F_{max} (x axis) = 0; thus, the predicted capacity is 5.559 e^{04} lbf. The actual capacity of the perfect cylinder is 6.450 e^{04} lbf that is 16 % more than the predicted capacity. This margin is quite satisfactory and gives confidence in the proposed algorithm. However, the real strength of the algorithm is tested by its application on imperfect cylinders. In the next section, we apply it to imperfect cylinders and evaluate its accuracy.

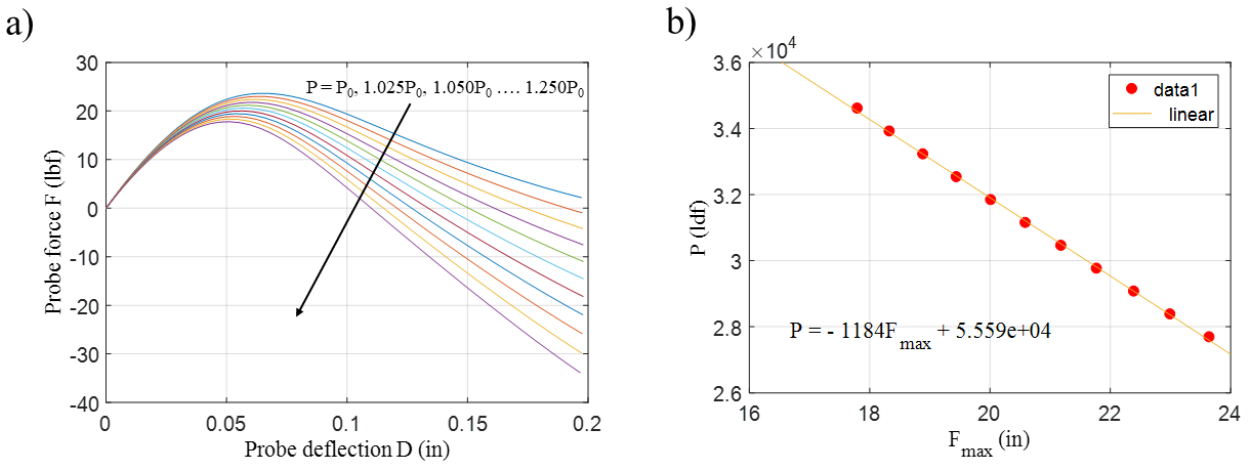

Figure 3: a) The plots between probing forces F and the probing displacements D for the 11 axially compressed perfect cylinders. b) The scatter plot between the maximum probing force F_{max} and corresponding prescribed axial compression along with the best fit line and its equation.

4. Application of the Algorithm on the Imperfect Cylinders

All real structures contain imperfections, and it is the capacity of imperfect cylinders that have been a nuisance for a long time. We do not know prior to the shape and size of the imperfections; and thus, knowing their capacity is difficult if not impossible. Consequently, designers must rely on conservative knockdown factor methods. In this section, we apply our proposed algorithm on imperfect cylinders and see if it is working well or not. For this purpose, we created two types of imperfect cylinders: first, single dimple imperfect cylinder, and second, double dimple imperfect

cylinder. Single dimple imperfect cylinder contains a single dimple, and double dimple imperfect cylinder contains two dimples.

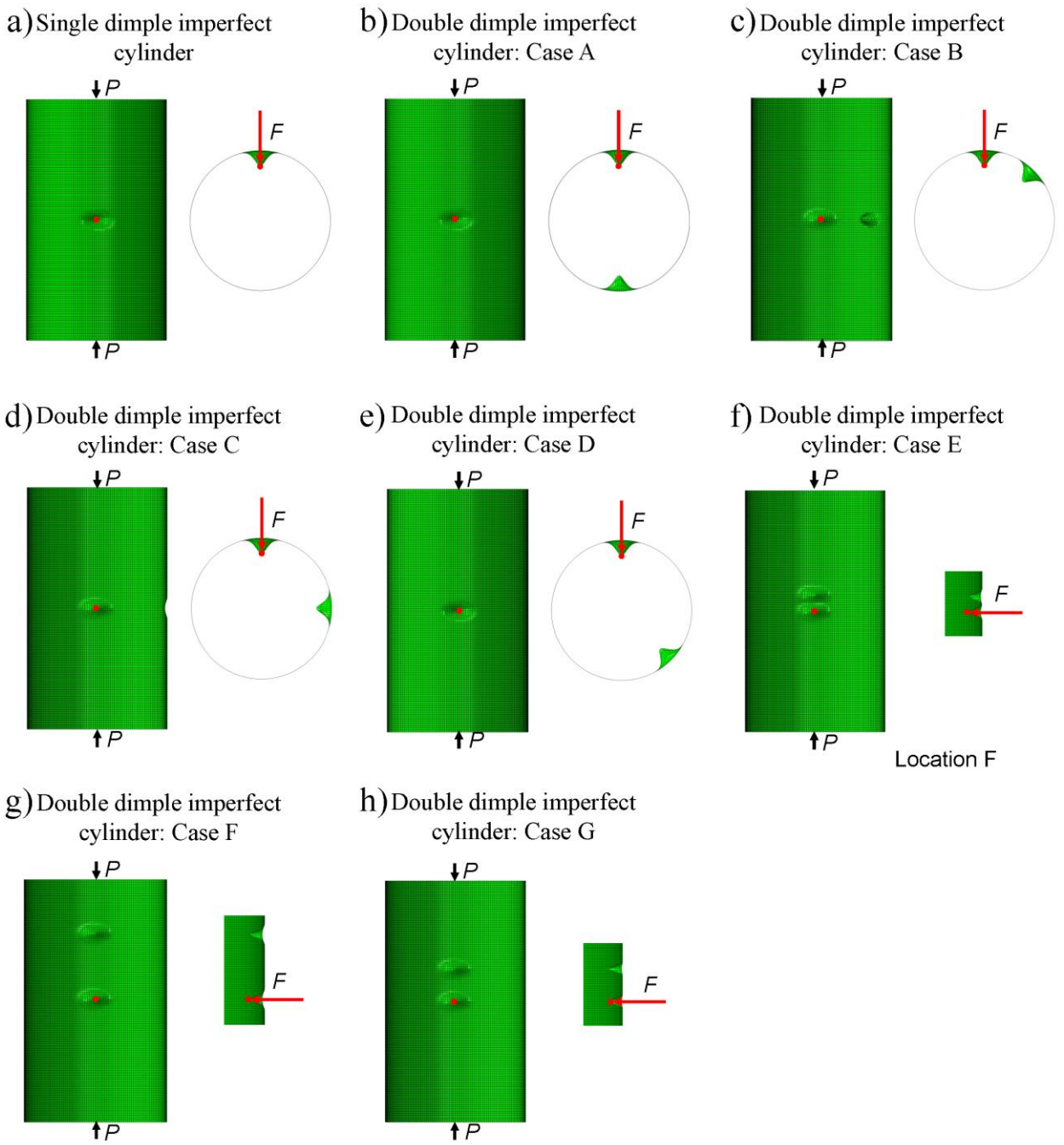

Figure 4: Single dimple imperfect cylinder (a), and seven double dimple imperfect cylinders with the varied relative location of the dimples (b, c, d, e, f, g, and h).

The mathematical expression of the dimple used in this study is (Gerasimidis et al. 2018):

$$w = w_0 e^{-\left(\frac{x}{x_1}\right)^2} e^{-\left(\frac{\theta}{\theta_1}\right)^2} \quad (2)$$

Where w represents the deviation of shell surface from its perfect position in the radial direction, and w_0 is the amplitude of the imperfection. x and θ are the axial and circumferential coordinates with the origin placed at the middle of the dimple's projection on the perfect cylinder's surface. x_1 and θ_1 are the parameters that decide the length (in the axial direction) and width (in the circumferential direction) of the dimple. The values for x_1 and θ_1 are chosen such that the length ($2x_1$) and the width ($2R\theta_1$) of the dimple are equal to the first eigenmode wavelength of the circular cylinder under axial compression, i.e. $3.44\sqrt{Rt}$ for $\nu = 0.3$ (Timoshenko et al. 1961). For single dimple imperfect cylinder, the dimple is placed in the middle of the cylinder as shown in Fig. 4a. For double dimple imperfect cylinder, the first dimple is placed at the middle of the cylinder, and the second dimple is placed at 7 different location as shown in Fig. 4b to Fig. 4h.

4.1 Prediction of single dimple imperfect cylinder's capacity

The application of Step I of the algorithm on the single dimple imperfect cylinder gives initial prescribed axial load P_0 = 4.628 e+04 lbf. This initial prescribed axial load P_0 is the input for Step II. In Step II, we must decide the location of the probing force. We apply the prob at 7 different paces as shown in Fig. 5 and Fig. 6: one in the middle of the dimple (Location 0), three at the middle of the cylinder but away from the dimple (Locations 1, 2 and 3), and three away from the middle of the dimple along the axial direction (Locations 4, 5 and 6). In this section we describe the case when probing is applied in the middle of the cylinder (Location 0); other cases will be discussed in the subsequent subsection.

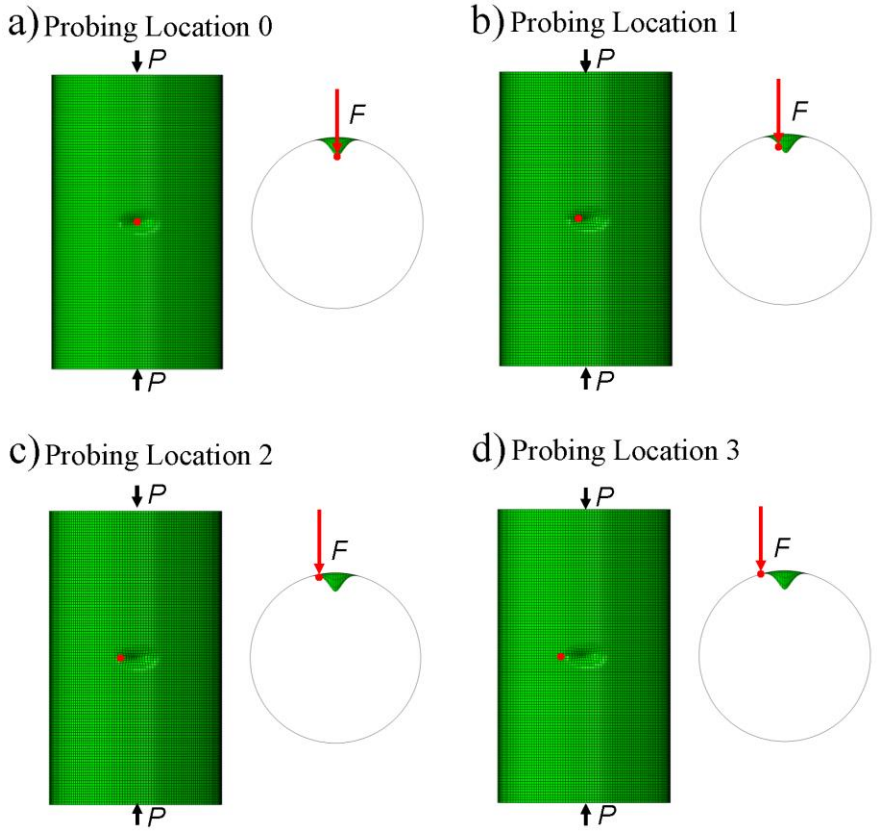

Figure 5: Various locations of probing force along the circumferential direction. Probing is in the middle of the dimple (Location 0), and the probing is in the middle of the cylinder but away from the middle of the dimple (Location 1, Location 2, and Location 3).

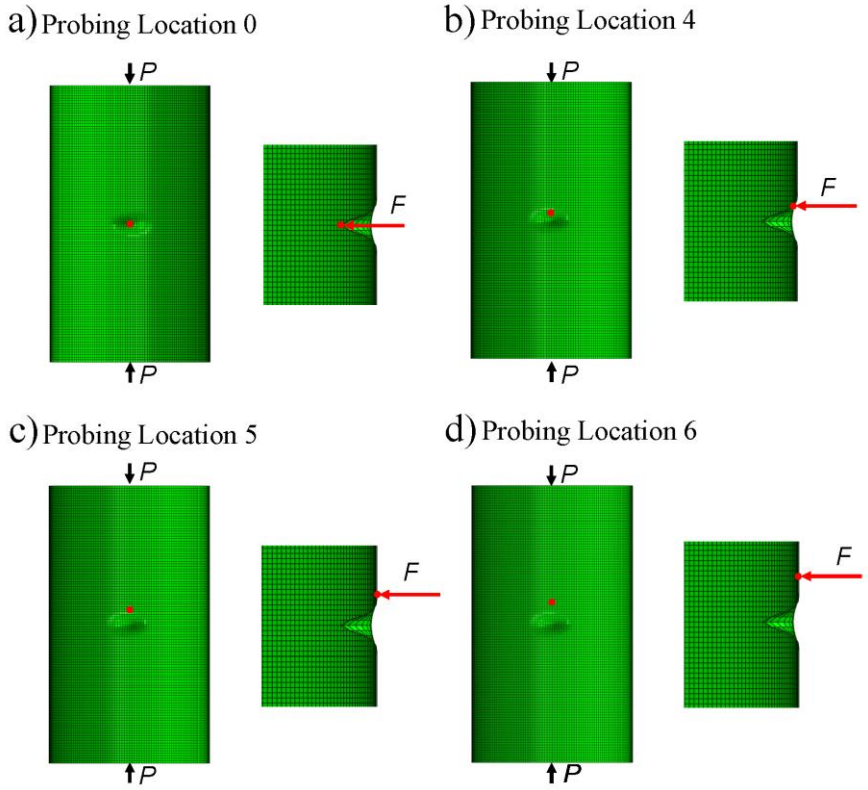

Figure 6: Various locations of probing force along the axial direction. Probing is at the middle of the dimple (Location 0) and probing along the axial direction away from the middle of the cylinder (Location 4, Location 5, and Location 6).

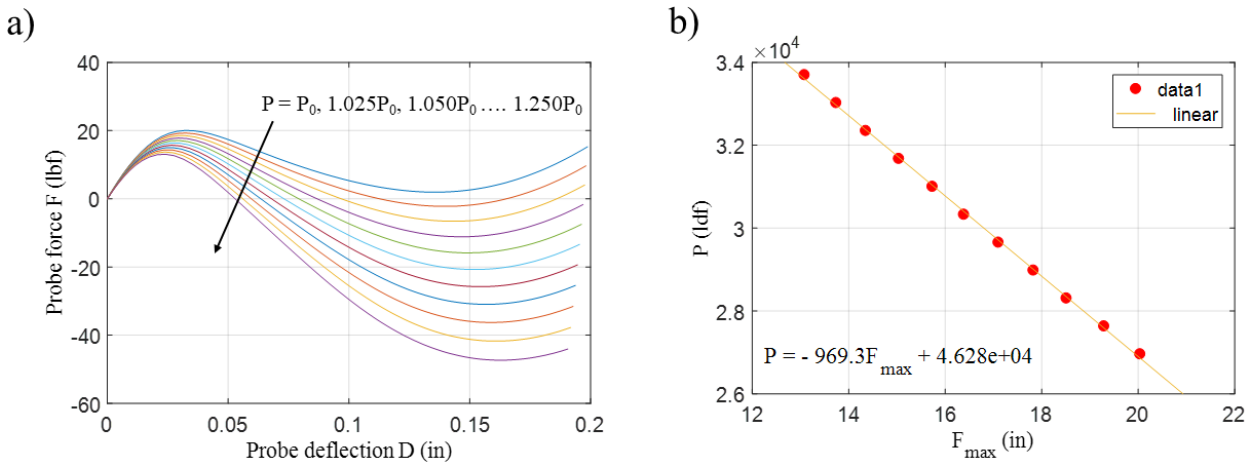

Figure 7: a) The plots between probing forces F and the probing displacements D for the 11 axially compressed single dimple imperfect cylinders. b) The scatter plot between the maximum probing force F_{max} and corresponding prescribed axial compression along with the best fit line and its equation.

In Step II, the cylinder is axially compressed under 11 different prescribed axial compression $P = (1 + .025)^0 \times P_0$, $(1 + .025)^1 \times P_0$, $(1 + .025)^2 \times P_0$, …. $(1 + .025)^{10} \times P_0$; thereafter, the probing force is applied at Location 0 of the 11 axially compressed cylinders. In Fig. 7a, the plots between probing forces F and the probing displacements D are drawn. Here again, the maximum probing force F_{max} is reducing with the increase of axial compression as expected. In Fig. 3b, scatter plot

is drawn between maximum probing force F_{max} and corresponding prescribed axial compression. These data are fitted by the line whose equation is:

$$P = -969.3F_{max} + 4.628\, e^{04} \quad (3)$$

The predicted capacity of the cylinder is the value of P (y axis) corresponds to the value of F_{max} (x axis) = 0 and is 4.628 e^{04} lbf. The actual capacity of the single dimple imperfect cylinder, found by nonlinear FEM analysis, is 4.975 e^{04} lbf—7.5 % more than the predicted capacity. So, our algorithm predicts the capacity very accurately if we apply the probing force in the middle of the imperfection. But, in all practical applications, the imperfection and its middle location are unknown; thus, the study of the location of probing is necessary. That is the subject of the next subsection.

4.2 Effect of the location of probing on the predicted capacity

To study the impact of the location of probing, 7 locations are chosen as shown in Fig. 5, and the proposed algorithm is applied for these 7 locations. The results are shown in Fig. 8 in the form of the ratio of predicted to actual capacity (y axis); the x axis does not represent any physical quality. A general pattern can be seen in this figure that is the predicted capacity is increasing as the probing location is moving away from the dimple. This is happening because the probing profile (probe force displacement plot) is not able to identify the characteristics of the imperfection when the probe is away from the imperfection.

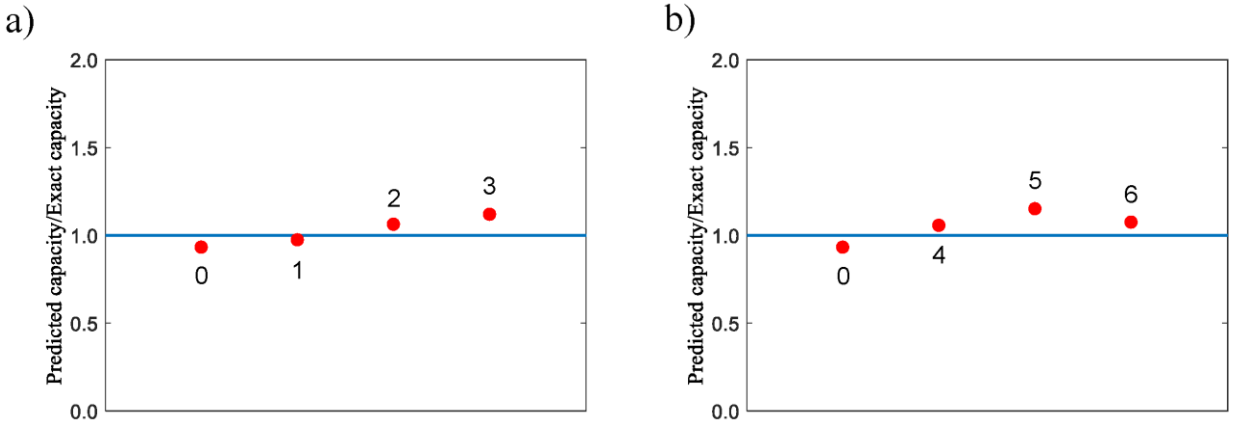

Figure 8: The effect of probing locations on the predicted capacity. (a) The probing location varies along the circumferential direction, and (b) probing location varies along the axial direction. The results are presented in the form of the ratio of predicted to actual capacity (y axis); the x axis does not represent any physical quantity, and the identity of the locations is represented by numbers 0, 1, 2, 3, 4, 5, 6, and 7.

Fig. 6a shows the effect of probing location along the circumferential direction, whereas Fig. 6b illustrates the effect of probing along the axial direction. For Location 0, the predicted capacity is minimum and less than the actual capacity; similarly, for Location 1, the predicted capacity is less than the actual capacity. For these two cases, the location of probing is inside the dimple; thus, the probing profile can capture the presence of the imperfection. For the other cases, i.e., Locations 2, 3, 4, 5, and 6, the predicted capacity is more than the actual capacity because the probing profile is not able to fully capture the imperfection. Nevertheless, there is not much difference among the predicted values irrespective of the probing locations. For example, the difference between the

predicted values is about 25 % (of predicted value by probing at Location 0) for Location 0 and Location 5. So, it can be concluded that the location of probing affects the predicted value, but not substantially. For practical applications, the probing can be done around 5 to 6 different places, and the average value of the predictions can be assumed as the capacity of the cylinder; this will remove the uncertainties associated with the location of the probing. In our example, the average value of the predicted values of 7 probing locations is 5.229 e^{04} lbf—5 % more than the actual capacity. So, if we applied our algorithm with multiple probing locations, the average of predicted values is quite a reasonable estimate of the cylinder's capacity.

4.3 Prediction the double dimple Imperfect cylinder's capacity

To test our proposed algorithm further, we implement it on the double dimple imperfect cylinder that contains two dimples as shown in Fig.5. First, we analyze the case A when the two dimples are located diametrically opposite direction at the middle of the cylinder, and the probing force is applied at the middle of the first dimple. The application of Step I of the algorithm results in the initial prescribed axial load P_0 = 4.594 e+04 lbf. In Step II, the cylinder is put under 11 different prescribed axial compression P = $(1 + .025)^0 \times P_0$, $(1 + .025)^1 \times P_0$, $(1 + .025)^2 \times P_0$, …. $(1 + .025)^{10} \times P_0$; thereafter, the probing force is applied at the middle of the first dimple. In Fig. 6a, the plots between probing forces F and the probing displacements D are drawn for the 11 axially compressed cylinders. Fig. 3b, a scatter plot is drawn between the maximum probing force F_{max} and corresponding prescribed axial compression. The data are fitted by the line whose equation is:

$$P = -948.1F_{max} + 4.594\, e^{04} \tag{4}$$

The predicted capacity of the cylinder is 4.594 e^{04} lbf that is the value of P (y axis) corresponds to the value of F_{max} (x axis) = 0. The actual capacity of the imperfect cylinder, found by FEM analysis, is 5.000 e^{04} lbf—9.00 % more than the predicted capacity. Again, our algorithm predicts the capacity quite accurately if we apply the probing force in the middle of the imperfection one dimple.

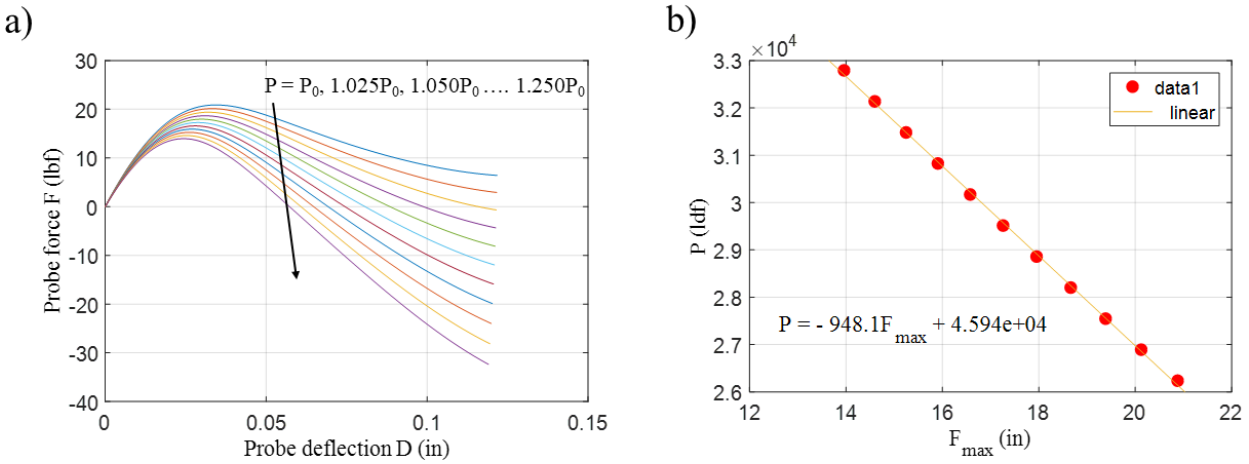

Figure 9: a) The plots between probing forces F and the probing displacements D for the 11 axially compressed double dimple imperfect cylinders when the two dimples are diametrically opposite direction. b) The scatter plot between the maximum probing force F_{max} and corresponding prescribed axial compression along with the best fit line and its equation.

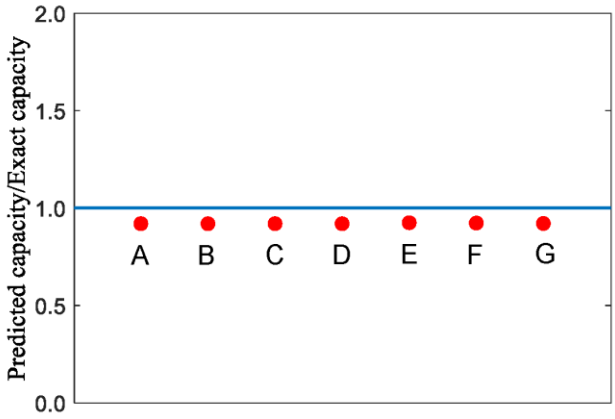

Figure 10: Effect of relative positions of the dimples on the predicted capacity for the double dimple imperfect cylinders.

For the other cases, i.e., B, C, D, E, F, and G of Fig. 5, the predicted values are illustrated in Fig. 10 in form of the ratio of predicted to actual capacity. In all the cases the first dimple is in the middle of the cylinder, while the location of the second dimple varies along the circumferential and longitudinal direction. The probing is always applied in the middle of the first dimple. The proposed algorithm predicts the same capacity in all cases. This means the relative location of two dimples does not influence the prediction if one of the dimples is in the middle of the cylinder and probing is applied in the middle of this dimple. The location of probing might affect the predicted capacity, but we have not yet studied the effect of probing locations for the double dimple imperfect cylinder. However, these results suggest the possibility that a procedure can be developed to predict the capacity of thin cylinders containing multiple dimple imperfections.

5. Conclusions

Thin cylindrical shells that are used in engineering applications always contain imperfections; as a result, their actual capacities are difficult, if not impossible, to determine. In this study, a new non-destructive method based on the energy barrier approach is proposed to determine the capacity of thins cylinders and is computationally validated. First, this method is applied to a perfect cylinder, which results in a 16 % accurate prediction. Further, this method is applied to two imperfect cylinders: single dimple imperfect, and double dimple imperfect cylinders. For the single dimple imperfect cylinder, the predicted capacity is 7.50 % accurate if the probing force is applied in the middle of the dimple. The location of the probing force affects predicted capacity but not substantially. For the double dimple imperfect cylinder, the prediction is 9 % accurate when the probing is applied in the middle of one dimple, while the other dimple is located diametrically opposite direction. The predictions are sufficiently accurate (with an accuracy of around 10 %) for the other combinations of two dimples. Our study is limited in many ways: the experiments have not been done for further verification, and only two types of imperfections are used. Nevertheless, the presented results are very promising and encouraging; experiments and additional studies will be done in the future to refine the proposed algorithm further.

References

ABAQUS manual 6.14-14. Dassault Systèmes Simulia Corp.

Fan H. (2019), "Critical buckling load prediction of axially compressed cylindrical shell based on non-destructive probing method." *Thin-Walled Structures*, 139 91-104.

Gerasimidis S., Virot E., Lee A., Hutchinson J.W., Rubinstein S.M. (2018), "On Establishing Buckling Knockdowns for Imperfection-Sensitive Shell Structures." *Journal of Applied Mechanics*, 85 (9) 091010.

Groh R.M.J., Pirrera A. (2019), "On the role of localizations in buckling of axially compressed cylinders." *Proceedings of the Royal Society A: Mathematical Physical and Engineering Sciences*, 475 20190006.

Hutchinson J.W., Thompson, J.M.T. (2017), "Nonlinear Buckling Interaction for Spherical Shells Subject to Pressure and Probing Forces." *Journal of Applied Mechanics*, 84 (6) 061001.

Hutchinson J.W., Thompson, J.M.T. (2018), "Imperfections and energy barriers in shell buckling." *International Journal of Solids and Structures*, 148-149 167-168.

Koiter, W. T. (1945). "On the stability of elastic equilibrium." *Thesis Deft, H.J. Paris, Amsterdam.*

Kreilos T., Schneider T.M. (2017), "Fully localized post-buckling states of cylindrical shells under axial compression." *Proceedings of the Royal Society A: Mathematical Physical and Engineering Sciences*, 473 20170177.

Lee A., Jiménez F.L., Marthelot J., Hutchinson J.W., Reis P.M. (2016), "The Geometric Role of Precisely Engineered Imperfections on the Critical Buckling Load of Spherical Elastic Shells." *Journal of Applied Mechanics*, 83 (11) 111005.

Marthelot J., Jiménez F.L., Lee A., Hutchinson J.W., Reis P.M. (2017), "Buckling of a Pressurized Hemispherical Shell Subjected to a Probing Force." *Journal of Applied Mechanics*, 84 (12) 121005.

Riks E. (1979), "An incremental approach to the solution of snapping and buckling problems." *International Journal of Solids and Structures*, 15(7) 529-551.

Sieber J., Hutchinson J.W., Thompson, J.M.T. (2019), "Nonlinear dynamics of spherical shells buckling under step pressure." *Proceedings of the Royal Society A: Mathematical Physical and Engineering Sciences*, 475 20180884.

Thompson, J.M.T. (2015), "Advances in Shell Buckling: Theory and Experiments." *International Journal of Bifurcation and Chaos*, 25 (01) 153001.

Thompson, J.M.T., Sieber J. (2016), "Shock-Sensitivity in Shell-Like Structures: With Simulations of Spherical Shell Buckling." *International Journal of Bifurcation and Chaos*, 26 (02) 1630003.

Thompson, J.M.T., Hutchinson J.W., Sieber J. (2017), "Probing Shells Against Buckling: A Nondestructive Technique for Laboratory Testing." *International Journal of Bifurcation and Chaos*, 27 (14) 1730048.

Timoshenko S. P., Gere J.M. (1961) Theory of elastic stability. McGraw-Hill.

Virot E., Kreilos T., Schneider T.M., Rubinstein S.M. (2017), "Stability Landscape of Shell Buckling." *Physical Review Letters*, 119 224101.